

See discussions, stats, and author profiles for this publication at: <https://www.researchgate.net/publication/5889937>

Nonradiative Resonant Excitation Transfer from Nanocrystal Quantum Dots to Adjacent Quantum Channels

ARTICLE *in* NANO LETTERS · DECEMBER 2007

Impact Factor: 13.59 · DOI: 10.1021/nl0719731 · Source: PubMed

CITATIONS

48

READS

10

2 AUTHORS, INCLUDING:



A. Madhukar

University of Southern California

380 PUBLICATIONS 10,606 CITATIONS

SEE PROFILE

Nonradiative Resonant Excitation Transfer from Nanocrystal Quantum Dots to Adjacent Quantum Channels

Siyuan Lu[†] and Anupam Madhukar^{*,†,‡}

Nanostructure Materials and Devices Laboratory, Department of Physics, and Mork Family Department of Chemical Engineering and Materials Science, University of Southern California, Los Angeles, California 90089-0241

Received August 8, 2007; Revised Manuscript Received September 21, 2007

ABSTRACT

Evidence is provided for *nonradiative* resonant energy transfer (NRET) from excitons in nanocrystal quantum dots (NCQDs) to the confined states of an adjacent quantum well (QW) at low excitation power and rate competitive with the quantum dot radiative decay. This indicates that NRET in optimized NCQD–QW/nanowire systems may provide a solar energy conversion approach with a viable tradeoff with the bottlenecks of charge carrier generation and/or transport to/in electrodes faced by excitonic solar cells.

Two dominant classes of semiconductor quantum nanostructures have emerged in the past couple of decades: (i) the vapor-phase deposition based planar^{1–4} and spatially templated (i.e., patterned^{5–7} or seeded)^{8–9} quantum nanostructures (wells, wires, and boxes/dots) of which the epitaxial planar quantum wells¹ and the lattice-mismatch strain-driven, spontaneously formed, coherent island based quantum dots^{2,3} are the most widely studied and utilized in devices such as transistors, light emitters, and detectors;⁴ (ii) the nanocrystal-based quantum dots, rods, and tetrapods, usually synthesized via solution chemistry routes,^{10,11} of which the nanocrystal quantum dots (NCQDs) have become most popular given their usefulness for biological and biomedical imaging applications in vivo and in vitro, including in platform-based assays.^{12–15} An earlier use of nanocrystals involved composites of dye-coated metal oxide nanocrystals of large sizes (where no quantum confinement effects are present) in a thick film, with the pores filled with liquid or solid electrolyte, which were shown to be promising for solar energy conversion.¹⁶ The dye molecules act as the solar photon absorption medium, and the choice of the relative alignment of their HOMO and LUMO energy levels with respect to those of the nanocrystal enables the rapid dissociation of the strongly bound exciton at the interface and transfer of the released electron across the interface to the nanocrystal film (that acts as the anode). The hole migrates to the cathode mediated

by a redox species provided by the electrolyte.¹⁶ In such so-called dye-sensitized solar cells, to overcome the extremely slow percolative movement of the electron through the oxide, dye-sensitized oxide nanowires with considerably higher electron mobility (but still around a few $\text{cm}^2 \cdot \text{V}^{-1} \cdot \text{s}^{-1}$) have begun to be examined as a replacement for the oxide nanocrystals.^{17,18} In contrast to the limited absorption range (typically 400–800 nm) of the dyes, the potential of solar light absorption over the broad spectrum from ~ 400 to 1500 nm provided by the tetrahedrally bonded semiconductor NCQDs of varying composition and size in the strong quantum confinement regime has led to investigation of nanocrystals as the absorbers in TiO_2 matrix¹⁹ or in a polymer matrix.^{20,21} However, the difficulty of rapid carrier extraction and the low mobility of charge in polymers is a challenging obstacle to overcome in the polymer-based approaches. Overcoming the bottlenecks of carrier separation (i.e., exciton transport to an interface and subsequent splitting) and/or transport to the collecting electrodes has thus remained a major obstacle in the quest for the realization of adequately efficient and cost-effective exciton solar cells (i.e., dye-sensitized cells, all-organic cells and inorganic–organic hybrid cells). An alternative approach utilizing type II band offset core–shell nanowires as the photon absorbers as well as the charge separation channel and charge carrier transport channel has recently been proposed based upon calculations of the electronic energies and charge distributions.²² This takes advantage of the built-in electric field generated upon electron–hole pair creation, playing the role of the p–n junction in an otherwise conventional semiconductor solar cell.

* Corresponding author. E-mail: madhukar@usc.edu. Telephone: 1-213-740-4323. Fax: 1-213-740-4333.

[†] Nanostructure Materials and Devices Laboratory, Department of Physics, University of Southern California.

[‡] Mork Family Department of Chemical Engineering and Materials Science, University of Southern California.

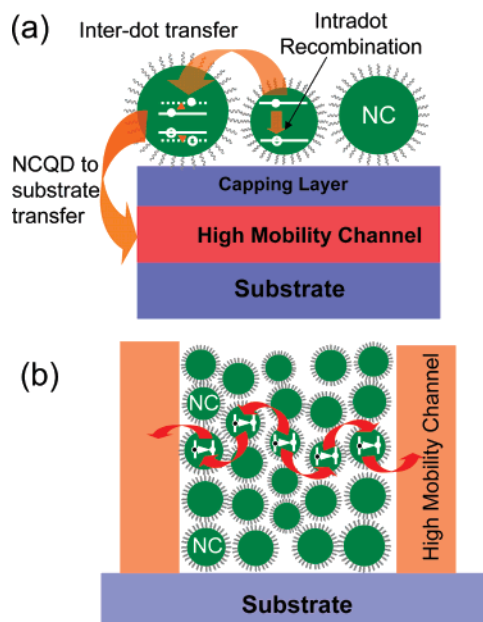


Figure 1. Schematic of (a) ligand-capped NCQDs deposited on near-surface epitaxial quantum nanostructure. Orange arrows indicate the competing intradot recombination, interdot nonradiative energy transfer, and NCQD-to-substrate nonradiative energy transfer processes; (b) nanocrystal absorbers dispersed in an array of appropriately designed high-mobility channels.

We present here an approach²³ that utilizes *nonradiative* coupling between transition dipoles for direct transfer of energy from the excitation created by light absorption in an absorber to carrier transport channels that can have charge mobilities in excess of $\sim 10^3 \text{ cm}^2 \cdot \text{V}^{-1} \cdot \text{s}^{-1}$.¹ To demonstrate the concept, it is convenient to place nanocrystal quantum dots as absorbers adjacent to semiconductor quantum wells (Figure 1a) and tailor the relevant energy levels of the NCQDs and the quantum well to achieve rapid nonradiative energy transfer to the transport channel. Such channels, quantum wells or wires, are provided by the technology of the planar¹ or spatially patterned epitaxial^{5–7} quantum wells and wires (Figure 1a) or chemically templated/seeded^{8,9} wires formed perpendicular to the substrate (Figure 1b). The convergence of these two classes of nanostructures, particularly the nanowire/NCQD composites in the configuration shown schematically in Figure 1b, provides a potentially cost-effective technology platform to realize the above-noted objectives. Indeed, any combination of absorber (inorganic or organic) with high-mobility transport channels (inorganic or organic) will suffice. But common to all material combinations and spatial architectures, the fundamental physical process to be examined then is the controlled *nonradiative* transfer of excitation energy from the NCQDs to nearby quantum wells and wires. This process is separate from carrier (electron or hole) transfer, or radiative energy transfer. It can be made fruitfully rapid in appropriately designed systems. Such platforms, we propose, could provide the building blocks of functional systems with architectures designed for a variety of applications ranging from solar energy conversion to detection of chemical, biochemical, or biological agents in the environment or in clinical applications.

In the following, we report on a system designed and synthesized to examine nonradiative excitation transfer from nanocrystal quantum dots (NCQDs) to an adjacent channel for carrier transport, here a near-surface epitaxially buried quantum well, at low excitation powers and present the first evidence for such transfer.²³ As shown by arrows in Figure 1a, NCQDs excited directly by an external light source can de-excite via (i) radiative decay, (ii) nonradiative transfer of energy to other NCQDs, (iii) nonradiative transfer to the “substrate” (i.e., adjacent nanostructures for collection and transport), and (iv) nonradiative decay with loss of energy to surroundings other than (ii) and (iii). The physical mechanisms for these channels compete with each other, and the challenge is to design and synthesize composite structures that optimize the desired processes (ii) and (iii). To place the studies reported here in the proper context of the literature, in the following, we provide first a brief recapitulation of the conceptual and historical context of the studies of nonradiative energy transfer from localized states to bulk solids. This is followed by considerations of the design and synthesis of the NCQD–epitaxial nanostructure system, the behavior of energy transfer, and a discussion of the results.

Energy Transfer between Molecules and Bulk Solids.

Historically, studies of nonradiative energy transfer between a molecule and a solid originated in response to Purcell’s prediction²⁴ in 1946 that the vacuum photon field induced spontaneous emission decay rate of an excited atom can be manipulated by changing this field around it. Before experimental investigations of this prediction could begin, Förster in 1948 showed²⁵ that the direct dipole–dipole interaction (i.e., no coupling with photon field) between molecules, which goes as the inverse third power of the separation (r) between the molecules, leads to nonradiative resonant energy transfer at a rate proportional to $(R_0/r)^6$, where R_0 is a characteristic distance at which the nonradiative transfer and radiative decay rates become equal and which thus measures the transfer efficiency. In the phenomenological Förster description R_0 , now called the Förster radius, is shown²⁶ to be proportional to the overlap of the emission and absorption spectral distributions of the donor and acceptor molecules, both of which can be measured. Values of R_0 between molecules range from ~ 1 –5 nm. The Förster mechanism has found an important place in molecular phenomena, including photosynthesis and certain biological processes. Pursuing Purcell’s prediction, in the late 1960s, Drexhage et al. investigated^{27,28} the radiative decay rate of an emitting molecule near a metal surface and found that it exhibits an oscillatory dependence on the molecule–metal distance. This distance dependence reflects the changing nature of the photon field at the molecule owing to the constructive and destructive interference between the electromagnetic field generated by the dipole of the emitting molecule and the field reflected by the metal surface. Since Drexhage’s confirmation of the Purcell effect, solid–molecule interaction studies have evolved into two major fields: (1) controlled enhanced emission from atoms and molecules in cavities (microwave and optical); indeed, the emergence of the epitaxial self-assembled quantum dots in the 1990s and their

placement in epitaxially grown microcavities has accelerated the now-active field of semiconductor cavity quantum electrodynamics;^{29,30} (2) the photophysics of molecules as a function of distance from surface, in particular beyond the findings of Drexhage in the far-field interaction regime which could be understood well by a classical electromagnetism (Maxwell's equations) based phenomenological theory developed by Chance, Prock, and Silbey (CPS) in the 1970s.³¹ The CPS description represented the solid by a dielectric function and the molecule as a point dipole. CPS found the nonradiative energy transfer rate to the metal to go as $(R_0/r)^n$, with $n = 3$, where R_0 is the Förster radius. For the semiconductor substrates of interest to our work reported here, a major step forward³² was taken by Stavola, Dexter, and Knox (SDK), who provided a quantum mechanical formulation of energy transfer from an excited molecule to underlying direct or indirect band gap semiconductor via excitation of electron–hole pairs. SDK derived³² the criterion $r \sim 7a$ as a reasonable transition regime between large and small separations, r being the perpendicular distance between the dipole and the solid surface and a the lattice constant of the solid. Analytical results for nonradiative energy transfer rate in the large separation regime could be extracted and showed the inverse cubic dependence found in the phenomenological theory of CPS. Indeed, this inverse cubic law could be anticipated by applying dimensional sum arguments to Förster's inverse sixth power law for transfer between two dipoles (molecules). Moreover, SDK showed that the presence of states localized at the surface restricts the sum of dipole–dipole interactions in the surface to two dimensions and thus gives rise to $n = 4$, i.e., an inverse fourth power law contribution.³² The first experimental study for semiconductor substrates was carried out by Alivisatos et al.³³ The authors showed that energy transfer from an adsorbed two-dimensional pyrene molecule overlayer to Si(111) substrate as a function of the thickness of an inert Xe spacer between the two can be modeled by the classical image dipole interaction as depicted by CPS at molecule–semiconductor separations greater than ~ 20 nm but, consistent with SDK, showed significant departure for distances < 3 nm.³³

Transfer between Localized States near Solid Surface and a Buried Semiconductor Nanostructure. Moving away from bulk solids, Basko et al.³⁴ theoretically examined resonant energy transfer from the one-dimensionally confined (i.e., two-dimensional) states in a semiconductor quantum well to the excited states of an adsorbed organic molecular noncrystalline overlayer and predicted efficient Förster energy transfer for separations on the order of 5 nm. However, to our knowledge, no experimental investigations of quantum well–molecule composite systems have been reported. Very recently, this idea has been applied to a study of electron and hole transfer from quantum well to an adsorbed nanocrystal quantum dot layer, motivated by the aim of demonstrating the potential of such hybrid structures for creating white-light-emitting diodes.^{35,36} Although electrical injection of the electrons and holes into the quantum well is the stated desired objective, optical pumping at extremely

high pump laser powers (MW/cm^2) was utilized to create the high carrier density ($10^{12}/\text{cm}^2$) in the quantum well required to demonstrate energy transfer to the NCQDs.³⁵ Our objective is the opposite: energy transfer *from* the NCQDs *to* the buried quantum well, and at low powers. For completeness, we note that excitation transfer between two localized epitaxial semiconductor nanostructures, such as coupled quantum wells and coupled quantum dots, has been examined and exploited for devices based on carrier tunneling.^{37,38} However, studies of excitation transfer between colloidal quantum nanostructures and buried epitaxial nanostructures are just beginning and the study of transfer *from* adsorbed nanocrystal quantum structures *to* buried nanostructures, as demonstrated below, is the first of its kind.

The Nanocrystal Quantum-Dot-Buried Quantum Nanostructure Composite Systems. Central to the desired energy transfer is controlling the relative position of the relevant energy levels of the constituents (called band or energy offsets) and the nature of the associated electronic charge distributions. For the most part, however, the energy offsets are not sufficiently accurately known and the electron affinity (or phototreshold) values of the constituents are customarily used and aligned with respect to a common vacuum level to mimic an overall potential defining the composite system. As our interest here is focused on nonradiative excitation transfer from the adsorbed NCQDs to buried quantum nanostructures, for the absolute transition energies of the major constituents, we have chosen the ground-state luminescence energy of the NCQD distribution (peak value ~ 965 nm for PbS NCQDs) to be larger than the gap of a buried quantum well (~ 1100 nm for an InGaAs well buried between GaAs) but yet smaller than the substrate band gap (873 nm for GaAs at room temperature). Their electron affinity rule based energy lineup is shown in Figure 2a, whereas Figure 2b indicates schematically the broadening of the ideally delta-function-like density of states of the NCQDs due to level broadening arising from their size fluctuation and the step-edge broadening of the two-dimensional electron and hole densities of states of the quantum well arising from the quantum well width and depth fluctuations. This arrangement permits exciting the NCQDs without exciting the GaAs substrate. The near surface quantum well (NSQW) is a GaAs/ $[(\text{InAs})_1(\text{GaAs})_2] \times 8/\text{GaAs}$ short period superlattice buried 10 ML (~ 3 nm) below the sulfur-passivated GaAs surface (Supporting Information Section S1). Its PL (Figure 3a) peak wavelength at ~ 1100 nm and full width at half-maximum of ~ 95 nm (97 meV) are tailored to act as suitable acceptors of nonradiative energy transfer from the spectral distribution, shown in Figure 3b to be 134 nm (181 meV), accompanying the size distribution of the donor PbS nanocrystal quantum dots (Supporting Information Section S1) used in the hybrid structures reported on here. We note that, given the weak binding energies (< 10 meV) of excitons in such quantum wells, the room-temperature PL emission is dominated by electron–hole pair emission.

To create the integrated NCQD-buried epitaxial nanostructure hybrid systems, we systematically examined³⁹ adsorption of the PbS NCQDs from solution on the above-

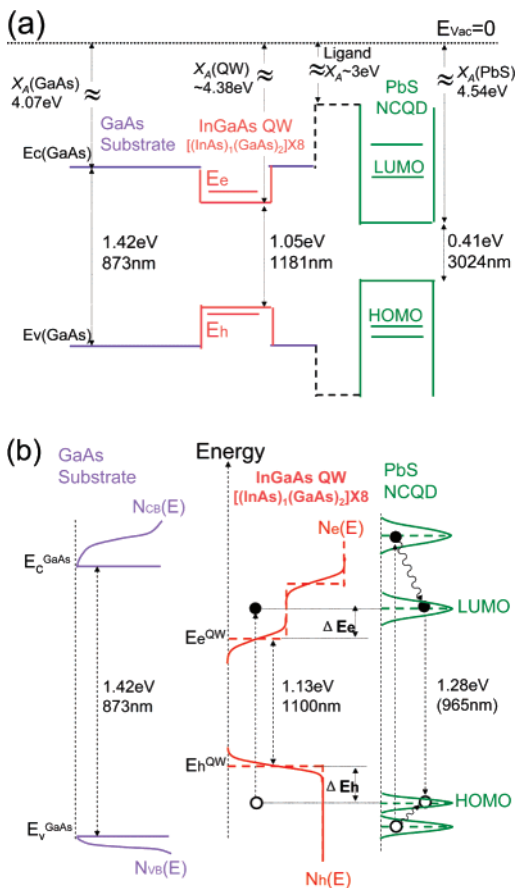


Figure 2. (a) Electron affinity (X_A) rule based alignment of the energy levels of the NCQDs, the ligands, the substrate, and the buried quantum well. Numerical values shown correspond to the system of PbS NCQDs on InGaAs QW buried in GaAs substrate utilized for the experimental findings reported here. (b) Schematic showing the energy levels and density of electron and hole states in our PbS NCQDs on an InGaAs QW buried GaAs substrate system. Note the broadening of the quantized electron and hole energy levels in the NCQDs and of the step rise in QW due to size or composition inhomogeneity.

noted sulfur-passivated GaAs surfaces with a particular focus on controlled deposition of only monolayer high NCQDs at submonolayer coverages characterized by atomic force microscopy (AFM). (Supporting Information Section S1). We have previously reported^{40,41} on the ability of the nanocrystals to retain their structural integrity when absorbed on a crystalline semiconductor substrate and potential consequences of even epitaxial overgrowth. The photoluminescence behavior of such adsorbed monolayers of PbS NCQDs on GaAs and glass substrates, normalized to the coverage, are shown in Figure 3b. In both cases, the PL from the PbS NCQDs is peaked at $\sim 965\text{ nm}$, sufficiently distant from the designed InGaAs NSQW emission peak at $\sim 1100\text{ nm}$. The overall PL for the NCQDs on GaAs substrate is $\sim 60\%$ of that from the NCQDs on glass substrate, consistent with the reduced local electric field effect arising from the different refractive indices (n) of the GaAs ($n = 3.5$) and glass ($n = 1.5$) substrates.⁴² Such samples were used for the studies of optical excitation transfer described in the following.

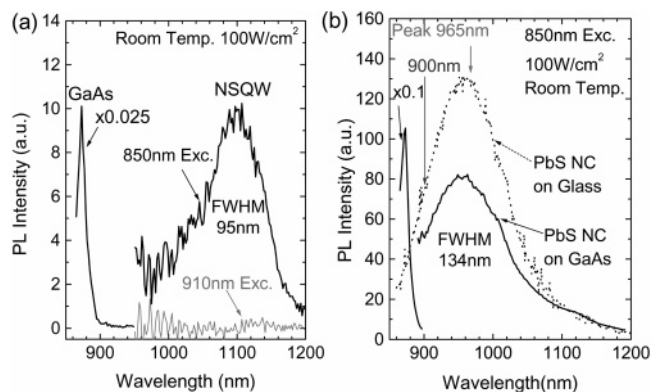


Figure 3. (a) Room-temperature PL from an GaAs/[(InAs)₁-(GaAs)₂]₈/GaAs near-surface quantum well (NSQW) buried 10 ML below the sulfur-passivated GaAs (line width $\sim 95\text{ nm}$ (97 meV)) at excitation 850 nm (black) and 910 nm (gray). Note the PL from NSQW at 910 nm excitation (below the GaAs band gap) drops below detection limit due to the lack of feeding from the GaAs substrate underneath. (b) Photoluminescence (normalized to the NCQD coverage) from a submonolayer of PbS NCQDs deposited on a glass substrate (dotted) and on a GaAs substrate (solid curve line width $\sim 134\text{ nm}$ (181 meV)).

Internanocrystal Quantum Dot Energy Transfer. The spectral distribution of the PL from NCQDs seen in Figure 3b is, of course, well-known to arise from the inhomogeneity of the NCQD size distribution. The NCQDs are spatially distributed on the surface at a local density such that significant inter-NCQD interaction, especially in the excited electronic states due to their more extended wavefunctions, can occur, inducing energy transfer from the smaller to the larger NCQDs. This skews the emission toward larger NCQDs. We have thus examined the interdot energy transfer behavior between the PbS colloidal nanocrystals utilizing time-resolved PL measurements (Supporting Information Section S2) on samples with PbS NCQDs deposited on glass, thus avoiding any ambiguity arising from the impact of the semiconductor surface. Figure 4a shows the room-temperature PL decay for detection at the NCQD PL peak (1.28 eV/965 nm) and at a higher energy (1.38 eV/900 nm) corresponding to the smaller NCQDs. Note the faster decay for the smaller NCQDs. We find that the PL decays are fit well only with a stretched exponential function, a form known to be suitable for transfer of energy between localized objects (here NCQDs) with fluctuating energy states in addition to fluctuations in interobject separation:^{33,43}

$$I_{\text{PL}}(t) = C + A \exp(-(t/\tau)^\beta) \quad (1)$$

The need for “stretched exponential” describes the presence of a superposition of exponentially decaying fluorescence intensities from a large number of NCQDs having a distribution of decay time constants $\{\tau_j\}$. Note that τ_j is a measure of the total decay rate of a set of nanocrystals, i.e., the sum of the decay rates due to intradot radiative and nonradiative processes, extradot nonradiative loss, and interdot Förster transfer. Also, note that the smaller the stretching exponent β , the broader the distribution of decay time constants $\{\tau_j\}$. As the measurement of intensity decay

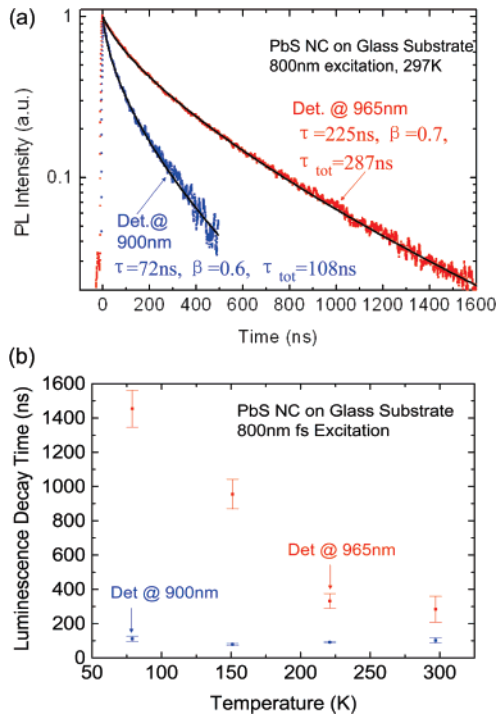


Figure 4. (a) Illustrative example of time-resolved PL of PbS NCs on glass substrate at 297 K, detected at the PL peak wavelength of 965 nm (red) and at 900 nm (blue). TRPL spectra are fitted with stretched exponential functions (black solid curves), which give mean total luminescence decay time (τ_{tot}) of 287 and 108 ns for emission at 965 and 900 nm, respectively, from the most probable and smaller size NCs. (b) Measured temperature dependence of the total luminescence decay time (τ_{tot}) detected at 965 nm (red) and 900 nm (blue). Note the decay time at 900 nm is limited to ~ 100 ns and independent of temperature, indicating rapid interdot energy transfer.

in eq 1 is for a narrow slice of the size distribution of the NCQDs defined by the chosen detection wavelength and window, a distribution of decay times manifested in β reveals the statistical variations in the immediate environment of the NCQDs, such as the number of passivating ligands, surface defects, and distribution of the size of the nearest neighbors. From such a distribution of individual decay times sampled at a given wavelength, a mean total decay time $\langle \tau_i \rangle$ can be calculated and is related to the parameters in eq 1 as:⁴⁴

$$\tau_{\text{tot}} = \langle \tau_i \rangle = \left(\frac{\tau}{\beta} \right) \Gamma\left(\frac{1}{\beta}\right) \quad (2)$$

where Γ represents the gamma function. We think this mean value is more representative of the physical behavior relevant to assessment of energy transfer rather than the time obtained in the stretched exponential fitting. Henceforth, therefore, reference to NCQD luminescence decay time extracted from TRPL measurements refers to τ_{tot} calculated from eq 2.

To shed further light on the measured decay time constant of the NCQDs, we examined the temperature dependence of the PL decay behavior of the ensemble. Figure 4b shows the temperature dependence of the extracted decay times. Note that the decay time of the larger NCQDs in the ensemble increases with decreasing temperature, whereas that

of the smaller NCQDs remains ~ 100 ns, essentially independent of the temperature. This indicates that the radiative lifetime of the smaller NCQDs is longer than the nonradiative excitation transfer time to the larger ones and the measurement is thus limited by this rapid transfer. The mechanism of such interdot transfer at the NCQD densities being examined here has been established previously⁴⁵ to be dominated by the Förster dipole–dipole interaction between primarily nearest-neighbor quantum dots even in thick films. Indeed, films created with NCQD size-ordered layer-by-layer deposition show a unidirectional flow of energy.⁴⁶ The Förster transfer rate (τ_{F}^{-1}) is well-known^{25,26} to be proportional to the radiative decay rate (τ_{rad}^{-1}) with a proportionality factor that, for point dipoles, can be represented as a power law (n) of the ratio of the Förster critical radius (R_0) and the separation (r) between the dipoles:

$$\tau_{\text{F}}^{-1} = \left(\frac{R_0}{r} \right)^n \tau_{\text{rad}}^{-1} \quad (3)$$

The radiative decay time is the rate when photon emission is the only decay mechanism and is given by $\tau_{\text{rad}}^{-1} = QE\tau_{\text{tot}}^{-1}$, where QE is the quantum efficiency of the NCQDs and τ_{tot}^{-1} is the measured total decay rate. For the PbS NCQDs used, the measured QE is $\sim 30\%$ (assuming that the QE of NCQDs deposited on the substrate is the same as NCQDs in toluene solution) and τ_{tot}^{-1} , measured at 965 nm for PbS NCQDs on glass, is $\sim (287 \text{ ns})^{-1}$. Thus the estimated radiative decay rate of PbS NCQDs is $\sim (960 \text{ ns})^{-1}$. Utilizing the well-known²⁶ expression for R_0 , for our experiments, we estimate⁴⁷ $R_0 = 5.9$ nm, while the center-to-center distance between the PbS NCQDs (accounting for the NCQD diameter of 2.5 nm and each NC coated with ligands ~ 1 nm in length) is $r = 4.5$ nm. The dense packing of the NCQDs indicates that the nearest-neighbor dipole–dipole interaction is the dominant contributor to energy transfer, and thus $n = 6$ power law in eq 3 is appropriate for interdot transfer, as also previously found for thick NCQD films.⁴⁵ The inter-NCQD Förster rate for NCQDs on the surface is then obtained to be $\sim (189 \text{ ns})^{-1}$, significantly higher (~ 5 times) than the NCQD intrinsic radiative decay rate ($\sim (960 \text{ ns})^{-1}$). This value is also consistent with the value $\sim (170 \text{ ns})^{-1}$ calculated directly from the difference of the rates $\sim (108 \text{ ns})^{-1}$ and $\sim (287 \text{ ns})^{-1}$ seen in Figure 4. The nearest-neighbor Förster transfer efficiency for the employed NCQDs having 30% quantum efficiency is thus $(170 \text{ ns})^{-1}/(108 \text{ ns})^{-1}$, $\sim 63\%$. With improvements in the chemistry of NCQD synthesis and surface functionalization, their quantum efficiency can be made near unity and thus the transfer efficiency will go up to $\sim 85\%$.

The central importance of the ratio of the inter-NCQD nonradiative transfer rate to the intra-NCQD radiative decay rate for the design of the NCQD-adjacent carrier transport channel system is that it governs the mean distance through the NCQD film over which resonant energy transfer to the NCQDs in direct contact with the channel may be realized. For a conservative estimate of this distance, taking our measured nearest neighbor transfer value of 63%, an on-

average transfer of 46% occurs for five NCQDs in a row. For quantum dots with near-unity quantum efficiency, starting with $\sim 85\%$ nearest-neighbor FRET, five nanocrystals would allow resonant transfer of energy with $\sim 74\%$ efficiency on average. For closest packing and typical NCQD diameter of say ~ 5 nm, this gives ~ 45 nm (i.e., nine linear NCQDs) as typical spacing between the exciton collection channels. This requirement needs to be balanced against the need for nanocrystal films of typically about a micrometer thickness to provide sufficient optical absorption path length to achieve essentially 100% photon absorption. Thus the conventional solar cell geometry, i.e., such a thick film sandwiched between two electrodes,^{17–19,48} is incompatible with effective *nonradiative* energy transport to the electrodes. In this geometry, very thin (< 50 nm) layers of NCQDs need to be sandwiched in a multilayer configuration, which would require benign repeated sequential deposition of the collection channels and NCQDs.^{41,48} Alternatively, a two-dimensional array of about a micrometer long quantum well/nanowire vertical channels spaced ~ 35 – 45 nm apart on an appropriate substrate with the space between them filled with NCQDs (Figure 1b) provides a more effective geometry. The generated excitons, having arrived at the collection channel by the FRET mechanism may, depending upon the chosen relative alignment of the HOMO–LUMO energies of the NCQD and the channel, transfer their energy via (a) exciton splitting into electron and hole with transfer of only one type of carrier and thus the attendant need for subsequent charge carrier transport in separate media or, (b) by NRET that directly generates an electron–hole pair in the same transport channel that is high mobility for both types. Next, we present studies of the excitation transfer process from NCQDs to adjacent quantum well.

NCQD to Quantum Well Excitation Transfer. Having established reference behavior of inter-NCQD excitation transfer within its own inhomogeneous size distribution, we next present our findings on excitation transfer between the NCQDs and underlying semiconductor substrates with and without buried quantum wells. Figure 5a shows the room-temperature time-integrated PL from two types of samples: PbS NCQDs on GaAs substrates without (solid curve) and with (dotted curve) near-surface buried InGaAs quantum well. Here the excitation wavelength is 850 nm, shorter than the room-temperature GaAs band gap wavelength of 872 nm. Thus, in addition to the excitons created by direct absorption by the PbS NCQDs and the quantum well, excitons are generated in the GaAs substrate, some of which feed to the buried quantum well, contributing to the observed emission at ~ 1100 nm. (Recall that the PL from the buried quantum well without NCQDs adsorbed is shown in Figure 3a). Note the reduction in the PL intensity from the NCQDs when going from substrates with no buried quantum well (solid curve) to substrates with buried quantum well (dotted curve).

To eliminate the feeding of the quantum well by the excitons generated in the GaAs substrate, we excited the samples at energies below the GaAs substrate band gap but above the NCQD HOMO–LUMO gap. An example is shown in Figure 5b for excitation at 910 nm. Once again,

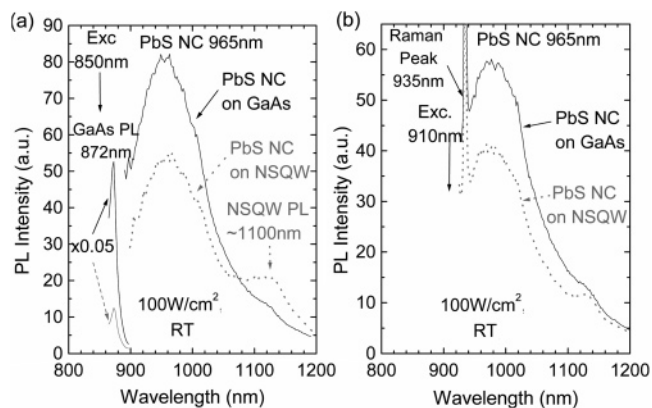


Figure 5. Room-temperature PL of PbS NCQDs on passivated GaAs (solid curve) and on passivated NSQW (dotted curve) excitation at 850 nm (panel a) and 910 nm (panel b), above and below the GaAs band gap at 873 nm, respectively. Data shown are the average of 10 PL measurements at 10 different spots on each sample.

the reduction in the NCQD PL seen below ~ 1120 nm in the presence of the buried quantum well establishes the presence of transfer of excitation from the NCQDs to the buried quantum well. Note also the correspondingly reduced QW luminescence at ~ 1100 nm, but which likely includes some contribution due to the radiative recombination of the electron–hole pairs generated by the NCQD exciton energy transferred to the buried epitaxial quantum well.

The transfer of the excitons from the NCQDs to the buried quantum well involves, at the minimum, excitons in the ground state of the NCQDs, i.e., the electrons and holes that have relaxed to their HOMO and LUMO states before excitation transfer to the quantum well. Energy conservation then demands that excited electron and hole states of the quantum well are involved. Such excited quantum well electrons and holes are well established⁴⁹ to relax to their respective ground states very rapidly (picoseconds), thus ensuring unidirectionality to the energy transfer. To shed light on the time scale and efficiency of such excitation transfer, we have examined the time-resolved behavior of the luminescence from the NCQDs adsorbed on quantum-well-containing substrates and compared it to the behavior on control substrates without the buried quantum well. Figure 6 shows the room-temperature time decay behavior of the luminescence peak of the NCQDs at 965 nm. Note the considerably fast decay time of ~ 208 ns in the presence of the quantum well as compared to the ~ 298 ns decay time on the GaAs control substrate. The reduction of the decay time to ~ 208 ns for the substrate with the buried near-surface quantum well is further manifestation of the opening of an excitation transfer channel provided by the one-dimensionally confined states of the quantum well (Figure 2b).

Discussion and Conclusion. As noted above, the measured reduction in the integrated PL intensity from PbS NCQDs on NSQW compared to PbS NCQDs on GaAs (Figure 5) is $\sim 35\%$. In the measured TRPL spectrum, the PL peak intensity after excitation light pulse is essentially the same for the two types of samples, testifying to the reproducibility of the NCQD distribution on the GaAs

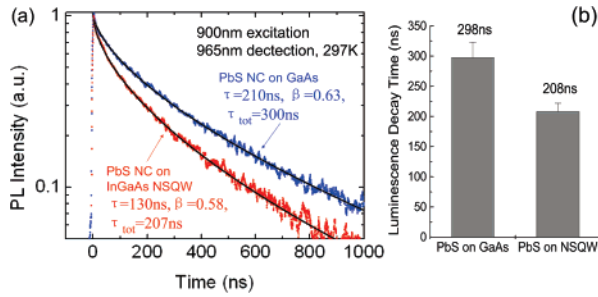


Figure 6. (a) Time-resolved PL of PbS NCs on passivated GaAs (blue) and on passivated NSQW (red), excited at 900 nm (below GaAs band gap) and detected at 965 nm (PbS PL peak). The decay of the TRPL curves are fitted using stretched exponential function. (b) Mean luminescence decay time (τ_{tot}) of PbS NCs (detected at 965 nm) on GaAs and on NSQW. Error bar shows the standard deviation of the measured decay times from five different spots on each sample.

surface. Defining the peak intensity as time $t = 0$, the NCQD HOMO–LUMO PL total decay rate in the presence of NSQW ($\tau_{\text{tot}}^{-1}(\text{NSQW}) = (208 \text{ ns})^{-1}$) is $\sim 40\%$ faster than on GaAs ($\tau_{\text{tot}}^{-1}(\text{GaAs}) = (298 \text{ ns})^{-1}$).

The total decay rate of the PbS NCQDs on NSQW bearing GaAs ($\tau_{\text{tot}}^{-1}(\text{NSQW}) = (208 \text{ ns})^{-1}$) can be written as the sum of NCQD total decay rate on GaAs without the buried QW ($\tau_{\text{tot}}^{-1}(\text{GaAs}) = (298 \text{ ns})^{-1}$) and the nonradiative transfer rate (τ_{NR}^{-1}) of excitons from PbS NCQDs directly to the NSQW:

$$\tau_{\text{tot}}^{-1}(\text{NSQW}) = \tau_{\text{tot}}^{-1}(\text{GaAs}) + \tau_{\text{NR}}^{-1} \quad (4)$$

Thus we calculate the nonradiative transfer rate τ_{NR}^{-1} to be $\sim (690 \text{ ns})^{-1}$. Recalling that the radiative decay rate (τ_{rad}^{-1}) of PbS NCQD is $\sim (960 \text{ ns})^{-1}$, we thus find the nonradiative energy transfer rate (τ_{NR}^{-1}) from the PbS NCQDs to the NSQW is ~ 1.4 times the radiative decay rate τ_{rad}^{-1} . For the PbS quantum dots used here having 30% quantum yield, this gives $\sim 30\%$ nonradiative resonant transfer efficiency to the NSQW channel. For near-unity quantum yield dots, it would be $\sim 60\%$. Note that the measured NCQD to NSQW transfer rate is seen to be about a quarter as fast as the measured rate $(170 \text{ ns})^{-1}$ for interdot Förster transfer from the small to the large NCQDs within in the densely packed NCQD monolayer. This is expected given the larger distance ($\sim 8.2 \text{ nm}$) of the NCQD monolayer from the underlying quantum well in the current concept-demonstration system. At such separation, FRET is likely the primary contributor to NRET. The SDK theory places the separation $\sim 8 \text{ nm}$ in the far-field regime. Thus utilizing for the transfer rate to a quantum well the Förster expression $\tau_{\text{F}}^{-1} = (R_0/r)^4 \tau_{\text{rad}}^{-1}$, the above-extracted transfer rate of $(690 \text{ ns})^{-1}$, measured radiative decay rate of $(960 \text{ ns})^{-1}$, and $r = 8.2 \text{ nm}$, we extract R_0 to be $\sim 8.9 \text{ nm}$ for the current PbS NCQDs on the InGaAs near-surface quantum well system.

Because the Förster energy transfer rate is proportional to the radiative transfer rate (eq 1), as long as the design of the composite NCQD–QW nanosystem maintains $(R_0/r) > 1$, the energy transfer rate to the QW will be faster than the

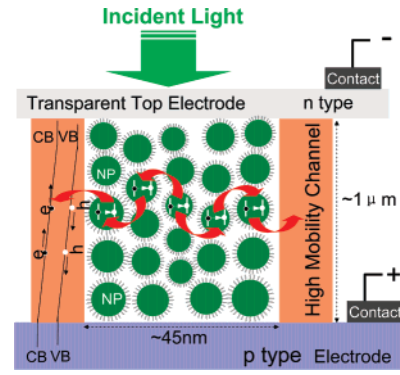


Figure 7. Schematic showing an architecture comprising nano-crystal absorbers embedded in a vertical array of high-mobility channels that allow nonradiative transfer of excitons from the adjacent NCQDs and simultaneously provide high-mobility transport.

intradot radiative decay rate. Of course, energy transfer occurs even otherwise. We note that R_0 depends on the wavelength of NCQD emission, the absorption cross-section of the NSQW, the spectral overlap between the NCQDs and the NSQW, and the quantum yield of the NCQDs.²⁶ In particular, R_0 is proportional to the NCQD emission wavelength. Hence, compared to the NCQDs in the visible spectrum (such as CdS, CdSe, CdSe/ZnS, etc.), the near-infrared (NIR) NCQDs (such as PbS, PbSe or InAs based) are even better suited for excitation transfer applications. Because their radiative decay rate represents the intrinsic rate-limiting step for the availability of excitons to transfer their energy, it is reasonable to expect that with the continued perfection of NCQD synthesis and improved QD quantum efficiency (through more effective surface passivation that reduces nonradiative recombination), the majority of the excitons created in the NCQDs can indeed be rapidly transferred to the NSQW before recombining radiatively within the NCQDs. As noted above, even for the NCQD–NSQW composite design involving $\sim 8.2 \text{ nm}$ separation between them employed in these first demonstration experiments, for near-unity quantum yield dots, the Förster transfer efficiency would be $\sim 60\%$. Reducing the separation to 6 nm would enhance the rate by a factor of ~ 4 and thus enhance the efficiency of the transfer to the channel to $\sim 84\%$.

Having established the feasibility of *nonradiative* transfer of energy absorbed by the NCQDs to adjacent quantum wells that are known to be structures that provide high carrier mobilities, we are motivated to examine a variety of appropriate architectures of nanocrystal-absorber–high-mobility transport channel integrated hybrid structures. The architectures may involve transfer to and collection from quantum wells in a planar geometry (horizontal, vertical, or inclined) or to two- or three-dimensional array of nanowires realized via vapor-phase growth and structural or chemical templating techniques. Recall that to achieve 100% photon absorption requires the NCQD film to be about a micrometer thick. An illustrative architecture is shown in Figure 7. It involves an appropriately designed array of charge transport channels with spacing optimized for desired level of on-average inter-NCQD NRET efficiency, as discussed in the

preceding. Our findings permit estimation of the range of overall efficiency expected from NRET-based solar cells for the 30% quantum yield NCQD employed in the current studies as well as for NCQDs of quantum yields near unity. The overall efficiency for the NRET-based solar cells involves the product of the efficiencies of the four processes involved. Two of these, common with other approaches, are the efficiency of collecting incident photons within the spectral range targeted and the efficiency of collecting the generated electron and hole charge carriers finally in the electrodes. The other two are the efficiency of (a) inter-NCQD nearest-neighbor NRET-based transfer (on average, $\sim 46\%$ for the current NCQDs and $\sim 74\%$ for unity quantum yield NCQDs for transfer through ~ 5 nanocrystals in a row) and (b) NRET from NCQD to the channel from the dots in direct contact with the channels ($\sim 30\%$ for the current NCQDs or 60% for NCQDs with unity quantum yield, respectively). The product of these two is the essence of what an optimized NRET-based cell could do. This is so because, for the other two processes involved, achieving effectively 100% photon absorption is possible in virtually any type of solar cell including this, and the collection efficiency of the electrons and holes created in a quantum well of such short channel lengths as about a micrometer, under bias, is essentially unity (as testified by the vast literature of QW photodetectors). Thus the product of these four numbers, multiplied by the Shockley–Queisser⁵⁰ thermodynamic limit of $\sim 30\%$ (for absorption centered at ~ 1 eV), gives $\sim 4\%$ or $\sim 13\%$ as the overall efficiency for our proposed solar cells employing NCQDs of, respectively, $\sim 30\%$ or $\sim 100\%$ quantum yield and transferring their energy via NRET to a channel ~ 8.2 nm away. Reducing this separation to 6 nm would enhance this range to 8% to 19%. Keeping in mind that the R_0 depends upon the physical size and the emission wavelength of the NCQDs and the NCQD-to-channel NRET efficiency on (R_0/r) , maximizing this ratio is at the core of the NRET-based single absorption channel solar conversion devices. This offers considerable opportunity for theoretical and experimental research on appropriate material combinations and structures. The challenge is to design architectures that incorporate multilayers of NCQDs of varying mean sizes and different chemical compositions that cover absorption over the extended UV, visible, and NIR regimes, each near appropriately tailored transport channels for efficient non-radiative resonant transfer of the absorbed energy. Such systems could provide a means of combining effective solar photon harvesting with acceptable rate of conversion of the created NCQD excitons into charge carriers and their subsequent rapid collection through high-mobility channels.

Acknowledgment. This research was supported by the DARPA/AFOSR funded Defense University Research Initiative in Nanotechnology (DURINT) program grant no. F49620-01-1-0474.

Supporting Information Available: Experimental details on (1) the synthesis of the nanocrystal quantum dot buried quantum nanostructure composite systems and (2) time-integrated and time-resolved photoluminescence measure-

ments. This material is available free of charge via the Internet at <http://pubs.acs.org>.

References

- (1) Weisbuch, C. Fundamental properties of III–V semiconductor two-dimensional quantized structures: the basis for optical and electronic device applications. In *Semiconductors and Semimetals: Application of Multiquantum Wells, Selective Doping, and Superlattices*; Dingle, R., Ed.; Academic Press: New York, 1987; Chapter 1. See also Weisbuch, C.; Vinter, B. *Quantum Semiconductor Structures*; Academic Press: New York, 1991.
- (2) Madhukar, A. Stress-Engineered Quantum Dots: Nature's Way. In *Nano-Optoelectronics*; Grundmann, M., Ed.; Springer Series in Nanoscience and Technology; Springer: New York, 2002; Chapter 2.
- (3) Shchukin, V.; Ledentsov, N. N.; Bimberg, D. *Epitaxy of Nanostructures*; Springer Series in Nanoscience and Technology; Springer, New York, 2003.
- (4) Bimberg, D.; Grundmann, M.; Ledentsov, N. N. *Quantum Dot Heterostructures*; Wiley & Sons: New York, 1999.
- (5) Madhukar, A. *Thin Solid Films* **1993**, 231, 8–42.
- (6) Konkur, A.; Madhukar, A.; Chen, P. *Appl. Phys. Lett.* **1998**, 72, 220–222.
- (7) Kiravittaya, S.; Heidemeyer, H.; Schmidt, O. G. *Physica E* **2004**, 23, 253–259.
- (8) Westwater, J.; Gosain, D. P.; Tomiya, S.; Usui, S.; Ruda, H. *J. Vac. Sci. Technol., B* **1997**, 15, 554–557.
- (9) Dick, K. A.; Deppert, K.; Karlsson, L. S.; Wallenberg, L. R.; Samuelson, L.; Seifert, W. *Adv. Funct. Mater.* **2005**, 15, 1603–1610; Zhong, Z. H.; Qian, F.; Wang, D. L.; Lieber, C. M. *Nano Lett.* **2003**, 3, 343–346; Kim, Y.; Joyce, H. J.; Gao, Q.; Tan, H. H.; Jagadish, C.; Paladugu, M.; Zou, J.; Suvorova, A. *Nano Lett.* **2006**, 6, 599–604.
- (10) See, for example, Alivisatos, A. P. *Science* **1996**, 271, 933–937.
- (11) Murray, C. B.; Norris, D. J.; Bawendi, M. G. *J. Am. Chem. Soc.* **1993**, 115, 8706–8715.
- (12) Bruchez, M.; Moronne, M.; Gin, P.; Weiss, S.; Alivisatos, A. P. *Science* **1998**, 281, 2013–2016.
- (13) Chan, W. C. W.; Nie, S. M. *Science* **1998**, 281, 2016–2018.
- (14) For recent reviews, see Chan, W. C. W.; Maxwell, D. J.; Gao, X.; Bailey, R. E.; Han, M.; Nie, S. *Curr. Opin. Biotechnol.* **2002**, 13, 40–46.
- (15) Rhyner, M. N.; Smith, A. M.; Gao, X. H.; Mao, H.; Yang, L. L.; Nie, S. M. *Nanomedicine* **2006**, 1, 209–217.
- (16) Oregan, B.; Gratzel, M. *Nature* **1991**, 353, 737–740.
- (17) Baxter, J. B.; Aydil, E. S. *Appl. Phys. Lett.* **2005**, 86, 053114–1–3.
- (18) Law, M.; Greene, L. E.; Johnson, J. C.; Saykally, R.; Yang, P. *Nat. Mater.* **2005**, 4, 455–459.
- (19) Yu, P.; Zhu, K.; Norman, A. G.; Ferrere, S.; Frank, A. J.; Nozik, A. J. *J. Phys. Chem. B* **2006**, 110, 25451–25454 and references therein.
- (20) Nozik, A. J. *Physica E* **2002**, 14, 115.
- (21) Gur, I.; Fromer, N. A.; Alivisatos, A. P. *J. Phys. Chem. B* **2006**, 110, 25543–25546.
- (22) Zhang, Y.; Wang, L.-W.; Mascarenhas, A. *Nano Lett.* **2007**, 7, 1264–1269.
- (23) Initial results on the resonant transfer from PbS NCQDs to InGaAs quantum well were reported in Madhukar, A.; Lu, S. MRS Fall Meeting, Symposium M7.7, Boston, November 29, 2006.
- (24) Purcell, E. M.; Torrey, H. C.; Pound, R. V. *Phys. Rev.* **1946**, 69, 37–38.
- (25) Förster, Th. *Annu. Rev. Phys.* **1948**, 2, 55–75; Förster, Th. *Discuss. Faraday Soc.* **1959**, 27, 7–17.
- (26) The critical radius for FRET is given by the following equation and parameters: $R_0^6 = (9000 \cdot \ln(10) \cdot \kappa^2 \cdot QE) / (128 \pi^5 n^4 N_A) \int_0^\infty (F_S(\tilde{\nu}) \epsilon_S(\tilde{\nu})) / (\tilde{\nu}^4) d\tilde{\nu}$, in which κ is a geometrical factor representing the relative orientation of the dipoles, QE the quantum efficiency of the nanocrystals, n the refractive index of the environment, N_A Avogadro's number, F_S the acceptor absorption, ϵ_S the donor emission, and $\tilde{\nu}$ the frequency.
- (27) Drexhage, K. H.; Fleck, M.; Kuhn, H.; Schafer, F. P.; Sperling, W. *Ber. Bunsen-Ges. Phys. Chem.* **1966**, 70, 1179; Drexhage, K. H. *J. Lumin.* **1970**, 1/2, 693–701.
- (28) Drexhage, K. H. In *Progress in Optics*; Wolf, E., Ed.; North Holland: New York, 1974; Vol. 12.
- (29) Yamamoto, Y.; Tassone, T.; Cao, H. *Semiconductor Cavity Quantum Electrodynamics*; Springer Tracts in Modern Physics; Springer: New York, 2000; Vol. 196.

- (30) Yoshie, T.; Scherer, A.; Hendrickson, J.; Khitrova, G.; Gibbs, H. M.; Rupper, G.; Ell, C.; Shchekin, O. B.; Deppe, D. G. *Nature* **2004**, *432*, 200–203.
- (31) Chance, R. R.; Prock, A.; Silbey, R. In *Advances in Chemical Physics*; Rice, S. A., Prigogine, I., Eds.; Wiley-Interscience: New York, 1978; Vol. 37, p 1.
- (32) Stavola, M.; Dexter, D.; Knox, R. *Phys. Rev. B* **1985**, *31*, 2277–2289.
- (33) Alivisatos, A. P.; Arndt, M. F.; Efrima, S.; Waldeck, D. H.; Harris, C. B. *J. Chem. Phys.* **1987**, *86*, 6540–6549.
- (34) Basko, D.; Rocca, G. C.; Bassani, F.; Agranovich, V. M. *Eur. Phys. J. B* **1999**, *8*, 353–362.
- (35) Achermann, M.; Petruska, M. A.; Kos, S.; Smith, D. L.; Koleske, D. D.; Klimov, V. I. *Nature* **2004**, *429*, 642–646.
- (36) Kos, S.; Achermann, M.; Klimov, V. I.; Smith, D. L. *Phys. Rev. B* **2005**, *71*, 205309.
- (37) Emiliani, V.; Ceccherini, S.; Bogani, F.; Colocci, M.; Frova, A.; Shi, S. S. *Phys. Rev. B* **1997**, *56*, 4807–4817.
- (38) Heitz, R.; Mukhametzhanov, I.; Chen, P.; Madhukar, A. *Phys. Rev. B* **1998**, *58*, R10151.
- (39) Lu, S. Ph.D. Dissertation, University of Southern California, 2006.
- (40) Konkar, A.; Lu, S.; Madhukar, A.; Hughes, S.; Alivisatos, A. P. *Nano Lett.* **2005**, *5*, 969–973.
- (41) Madhukar, A.; Lu, S.; Konkar, A.; Hughes, S.; Alivisatos, A. P. *Nano Lett.* **2005**, *5*, 479–482.
- (42) The CPS theory based calculated apparent quantum yield of the NCQDs on the GaAs substrate is 53% of that on glass. In this calculation, the parameters we used are: NCQD center-to-substrate distance, 3 nm, refractive indices of GaAs and glass, 3.5 and 1.5, respectively, at 965 nm (the peak of NCQD PL distribution), and the NCQD quantum yield (in the absence of a substrate) measured to be 30%.
- (43) Palmer, R. G.; Stein, D. L.; Abrahams, E.; Anderson, P. W. *Phys. Rev. Lett.* **1984**, *53*, 958–861; Doba, T.; Ingold, K. U.; Siebrand, W.; Wildmann, R. A. *Chem. Phys. Lett.* **1985**, *115*, 51–54.
- (44) Lindsey, C. P.; Patterson, G. P. *J. Chem. Phys.* **1980**, *73*, 3348–3357.
- (45) Kagan, C. R.; Murray, C. B.; Nirmal, M.; Bawendi, M. G. *Phys. Rev. Lett.* **1996**, *76*, 1517–1520; Fisher, B. R.; Eisler, H.-J.; Stott, N. E.; Bawendi, M. G. *J. Phys. Chem. B* **2004**, *108*, 143–148.
- (46) Franzl, T.; Klar, T. A.; Schietinger, S.; Rogach, A. L.; Feldmann, J. *Nano Lett.* **2004**, *4*, 1599–1603.
- (47) The critical radius for FRET from smaller (900 nm emission) PbS NCQD on glass to surrounding larger NCQDs is estimated to be $R_0 = 5.9$ nm using the equation given in ref 26 and the following parameters: the molar absorption coefficient of nanocrystals at 900 nm is measured to be $0.14 \times 10^5 \text{ M}^{-1} \text{ cm}^{-1}$, the nanocrystals are randomly orientated and thus $\kappa = 2/3$, the refractive index (n) of the environment is taken as 1.25 (the average dielectric constant of air and glass), and the quantum efficiency (QE) of the nanocrystals is taken the same as in solution: $\sim 30\%$ at room temperature.
- (48) Koeppe, R.; Bossart, O.; Calzaferri, G.; Sarisitsci, N. S. *Sol. Energ. Mater. Sol. Cells* **2007**, *91*, 986–995. After the preparation of the manuscript, we became aware of the very recent appearance of this paper, which reports finding a reduction in PL from CdSe/ZnS core–shell NCQDs buried in the smaller band gap ZnPc (zinc-phthalocyanine) film. It thus suggests the use of NCQDs and interdot nonradiative transfer to a smaller gap back electrode in solar cells.
- (49) Othonos, A. *J. Appl. Phys.* **1998**, *83*, 1789–1830; Lutgen, S.; Kaindl, R. A.; Woernerl, M.; Elsaesser, T.; Hase, A.; Kunzel, H.; Gulia, M.; Meglio, D.; Lugli, P. *Phys. Rev. Lett.* **1996**, *77*, 3657–3660.
- (50) Shockley, W.; Queisser, H. J. *J. Appl. Phys.* **1961**, *32*, 510–519.

NL0719731